Dalton Transactions

ROYAL SOCIETY OF CHEMISTRY

PAPER

View Article Online
View Journal | View Issue

Cite this: *Dalton Trans.*, 2025, **54**, 9270

Polyoxometalate-based complex@graphene composite electrodes for efficient nitrate reduction to ammonia†

Nan Zhao,[a] Xinming Wang, *[a] Shuang Rong,[b] Qiushuang Jiang,[a] Haoyun Li,[a] Haijun Pang *[a] and Huiyuan Ma[a]

Received 12th March 2025,
Accepted 8th May 2025

DOI: 10.1039/d5dt00597c

rsc.li/dalton

To replace the energy-intensive and polluting traditional ammonia synthesis process, in this study, we designed two polyoxometalate (POM)-based nickel/cobalt metal–organic composite catalysts, namely $(HNCP)_2[Ni(H_2O)_4]_2[NiMo_{12}(HPO_4)_4(PO_4)_4O_{30}]$ (Ni-P_4Mo_6) and $(HNCP)_2[Co(H_2O)_4]_2[CoMo_{12}(HPO_4)_4(PO_4)_4O_{30}]$ (Co-P_4Mo_6). These catalysts utilized {P_4Mo_6} as the structural unit, nickel/cobalt as the metal node, and π-conjugated organic ligands as the linkers, and they were loaded onto graphene oxide (GO) to enhance the conductivity and reaction contact area. Experimental results showed that in acidic electrolytes, Ni-P_4Mo_6/GO achieved an ammonia yield of 2.62 mg h^{-1} $mg^{-1}_{cat.}$ at −0.6 V (*vs.* RHE) with a faradaic efficiency (FE) of 83.9% at −0.5 V, outperforming Co-P_4Mo_6/GO (1.63 mg h^{-1} $mg^{-1}_{cat.}$ at −0.7 V; FE 85.3% at −0.3 V). Under neutral conditions, both the catalysts exhibited significantly improved performances (Ni-P_4Mo_6/GO: 11.6 mg h^{-1} $mg^{-1}_{cat.}$ yield, 88.4% FE; Co-P_4Mo_6/GO: 11.1 mg h^{-1} $mg^{-1}_{cat.}$ yield, 78.5% FE), surpassing most comparable catalysts. This work provides a novel strategy for developing efficient electrocatalysts for nitrate reduction to ammonia (e-NO_3RR).

1. Introduction

As an important carrier and energy storage intermediate in the carbon neutralization industry, ammonia is considered to be a future fuel substitute and plays a vital role in various industries such as leather, papermaking and agricultural fertilizer production.[1–6] The production of ammonia has been mainly dependent on a macroscale synthesis technology using the Haber–Bosch technique since 1913; however, its thermodynamic constraints—requiring extreme conditions (400–500 °C, 15–25 MPa) to overcome the high activation energy barrier of N≡N bond dissociation—result in massive energy consumption.[7–11] In contrast, the electrocatalytic nitrate reduction reaction (e-NO_3RR) for the synthesis of ammonia uses renewable electricity to drive the eight-electron reduction process, which can operate at room temperature and atmospheric pressure, and it is more thermodynamically inclined to choose nitrate rather than inert N_2 as the nitrogen source.[12–16] The electrocatalytic reduction of NO_3^- to NH_3 is an efficient process for transforming nitrate into the more valuable compound, NH_3. The conversion of NO_3^- can not only directly mitigate the problem of NO_3^- water pollution but also realize the green synthesis of ammonia. As a result, this reaction is regarded as one of the most potential methods for the eco-friendly and continuous production of ammonia in the future.[17–22] However, the e-NO_3RR faces enormous challenges such as reduced catalytic activity, low selectivity, and low ammonia production rate.[23] Therefore, developing cost-effective catalysts with high efficiency is crucial for overcoming these bottlenecks.[24–27]

So far, various catalysts have been developed for the e-NO_3RR. Among them, non-metallic catalysts have the characteristics of cost-effectiveness, strong electronic structure, adjustability and durability. However, the catalytic activity of non-metallic catalysts used in the e-NO_3RR is not satisfactory.[28] Noble metal catalysts are the most common high-activity electrocatalysts including ruthenium (Ru), rhodium (Rh) and platinum (Pt).[29–32] Nevertheless, the high cost and scarcity of resources have limited their further application. In contrast to noble metals, transition metal catalysts, along with their various compounds, such as oxides, sulfides, carbides, phosphides, and nitrides, provide unique performance advantages.[33–35] These materials have gained significant atten-

[a]*Key Laboratory of Green Chemical Engineering and Technology of College of Heilongjiang Province, School of Materials Science and Chemical Engineering, Harbin University of Science and Technology, Harbin 150040, P. R. China. E-mail: wangxinming20@126.com*
[b]*Heilongjiang Electric Power Research Institute, State Grid, Harbin 150030, P. R. China*

† Electronic supplementary information (ESI) available. See DOI: https://doi.org/10.1039/d5dt00597c

tion, especially in the field of e-NO_3RR.[36–38] For example, Cu/2D-CuO_x, Co/TiO_2 NSs and $Ni(OH)_2$@Ni show excellent electrocatalytic performance.[39–42]

Polyoxometalates (POMs) are a prominent category of inorganic compounds composed of numerous metal atoms interconnected through oxygen bridges, which are usually composed of highly oxidized transition metals (mainly W, V and Mo) with d^0 or d^1 electronic configurations.[43–47] Because of its reversible redox properties, diverse and controllable structural composition, it has great potential in catalysis, photochemistry, nanotechnology, medicine and other fields.[48,49] Nevertheless, the limited conductivity, tendency to agglomerate, and poor water solubility of POMs restrict their use in electrocatalysis. The construction of POMs–based metal–organic complexes can effectively ameliorate the aforementioned problems.[50] The Khalaji-Verjani team synthesized a PMo_{11}-Ru $(acac)_3$ electrocatalyst, showing high HER activity and stability.[51] Yang *et al.* developed two novel polyoxometalate-based metal–organic complexes through a self-assembly approach to link polyoxometalate clusters with CuCTC, which served as purpose catalysts, enabling both the electrochemical sensing and photocatalytic conversion of Cr(VI). The rates of Cr (VI) photoreduction achieved with these complexes outperformed those of Cu_3 and most other reported catalysts.[52]

In the family of POMs, the $[P_4Mo^V{}_6O_{31}]^{12-}$ ($\{P_4Mo_6\}$) anion has a stable structure with minimal steric hindrance and a rich array of active oxygen atoms. It can have a good synergistic effect with metal active sites and organic ligands, which gives $\{P_4Mo_6\}$ good topological scalability. Notably, the molybdenum in the structure is in pentavalent reduced state (Mo^V), which is an excellent electron donor. This unique characteristic can be leveraged as a potential "electron-donating unit" to pair with catalytically active species.[53–55] Therefore, the integration of $\{P_4Mo_6\}$ with composite materials could potentially establish an optimized catalytic framework, enhancing electron transport dynamics while improving both reaction efficiency and product specificity in nitrate reduction (NO_3RR) for ammonia synthesis.

Based on the above analysis, we selected the $\{P_4Mo_6\}$-type anion as the basic structural unit, nickel (Ni) and cobalt (Co) metal ions as nodes, and 2-(4-(4-carboxyphenyl)phenyl) imidazo(4,5-*f*)-(1,10)-phenanthroline (HNCP) with a large π-conjugated system as the organic ligand to construct two $\{P_4Mo_6\}$ polyoxometalate-based metal–organic complexes, $(HNCP)_2[Ni(H_2O)]_2[NiMo_{12}(H_2PO_4)_6(PO_4)_2(OH)_6O_{24}]$ (Ni-P_4Mo_6) and $(HNCP)_2[Co(H_2O)]_2[CoMo_{12}(H_2PO_4)_6(PO_4)_2(OH)_6O_{24}]$ (Co-P_4Mo_6), which was anchored onto functionalized graphene oxide (GO) substrates to obtain Ni-P_4Mo_6/GO and Co-P_4Mo_6/GO composites. The structural integration of graphene within the composite architecture significantly boosts the electrical conductivity and surface area, enhances the charge transfer kinetics for improved composite dispersion, and optimizes active site utilization to maximize the electrocatalytic performance.[56–59] Ni-P_4Mo_6/GO and Co-P_4Mo_6/GO composites show superior electrocatalytic efficacy in nitrate-to-ammonia conversion and stability, reaching the apex of NH_3 yield of 11.6 mg h^{-1} $mg^{-1}{}_{cat}$ and 11.1 mg h^{-1} $mg^{-1}{}_{cat.}$ and Faraday efficiency of 88.4% and 78.5% at −1.0 V in neutral electrolytes, respectively. Our findings propose a rational design framework for polyoxometalate-integrated catalytic systems, achieving unprecedented faradaic efficiency in sustainable ammonia synthesis *via* nitrate electroreduction.

2. Experimental section

2.1 Preparation of $(HNCP)_2[Ni(H_2O)_4]_2[NiMo_{12}(HPO_4)_4(PO_4)_4O_{30}]$ (Ni-P_4Mo_6)

A mixture of $[(NH_4)_6Mo_7O_{24}{\cdot}4H_2O]$ (0.85 g), ($NiCl_2{\cdot}6H_2O$) (0.40 g), HNCP (0.05 g) and CH_3CH_2OH (10 mL) was stirred for 10 min, and then deionized water (40 mL) and H_3PO_4 were added, respectively, with continuous stirring for 60 min. The pH value was adjusted to 1.0–1.5 with 1.0 M HCl or NaOH, and then the suspension was transferred to a 20 mL Teflon-lined autoclave and kept at 180 °C for 5 days. After slow cooling to room temperature at a rate of 10 °C h^{-1}, yellow diamond crystals were obtained (yield 65% based on Mo).

2.2 Preparation of $(HNCP)_2[Co(H_2O)_4]_2[CoMo_{12}(HPO_4)_4(PO_4)_4O_{30}]$ (Co-P_4Mo_6)

The compound Co-P_4Mo_6 was prepared following the same procedure as that of compound Ni-P_4Mo_6 except that $NiCl_2{\cdot}6H_2O$ (0.40 g) was replaced with $CoCl_2{\cdot}6H_2O$. Following gradual cooling at a rate of 10 °C h^{-1} until reaching room temperature, yellow-brown rhombic crystals of Co-P_4Mo_6 were obtained (yield 55% based on Mo).

2.3 Preparation of Ni-P_4Mo_6/GO

A mixture of Ni-P_4Mo_6 (0.50 g) and 50 mL deionized water was ultrasonicated for 3 h. Then, GO (0.25 g) and polyethyleneimine (C_2H_5N) (10 μL) were added and stirred for 30 min. The dispersion was washed with deionized water and centrifuged at 8000 rpm. After vacuum freeze-drying, a black fluffy powder was obtained (yield 40% based on Mo).

2.4 Preparation of Co-P_4Mo_6/GO

Co-P_4Mo_6/GO was prepared following the same procedure as that of Ni-P_4Mo_6/GO except that Ni-P_4Mo_6 (0.50 g) was replaced with Co-P_4Mo_6 (0.50 g). After vacuum freeze-drying, a black fluffy powder was obtained (yield 40% based on Mo).

2.5 Characterization

Fourier transform infrared (FTIR) spectra were recorded using a Bruker Tensor II spectrometer (Bruker, Germany) in the range of 4000–400 cm^{-1} by a KBr tablet method. X-ray powder diffraction (PXRD) was performed using a Rigaku D/max-TTR-III diffractometer with Cu-Kα-ray irradiation. The scanning speed was 5° s^{-1} and the measurement range was 5–50°. X-ray photoelectron spectroscopy (XPS) spectra were recorded at room temperature using a 12 kV and 20 mA Al Kα X-ray source by VG ESCALAB MK (VK, UK). The surface structure and morphology of the samples were characterized by trans-

mission electron microscopy (TEM) (JEOL, JEM-2010, 200 kV) and field emission scanning electron microscopy (FE-SEM) (Hitachi, SU 8000). Energy-dispersive spectroscopy (EDS) spectra were recorded by ensemble measurements using an SEM and a TEM. Ultraviolet–visible (UV-vis) spectra were recorded using a Shimadzu UV-1601 spectrometer in the wavelength range of 550–800 nm. Electrochemical tests were performed using a three-electrode system in a CHI 760E electrochemical workstation (Shanghai Chenhua).

3. Results and discussion

3.1 Preparation of composite catalyst materials

Ni-P_4Mo_6/GO and Co-P_4Mo_6/GO composite catalysts were synthesized for the e-NO_3RR (Scheme 1). The composite materials were mainly synthesized in two steps. First, crystal materials Ni-P_4Mo_6 and Co-P_4Mo_6 were prepared *via* a one-pot hydrothermal approach, and they were loaded onto graphene oxide (GO) to obtain Ni-P_4Mo_6/GO and Co-P_4Mo_6/GO.

3.2 Morphology and structure characterization of samples

The morphology and composition of the two prepared catalysts were analyzed by transmission electron microscopy (TEM) and scanning electron microscopy (SEM). The TEM result confirmed that the particles of the complex were distributed on the surface of the lamellar layers (Fig. 1 and Fig. S1†). The SEM images showed that the overall morphologies of Ni-P_4Mo_6/GO and Co-P_4Mo_6/GO are similar, both showing the lamellar morphology of GO (Fig. S2a and S3a†). The energy-dispersive X-ray spectroscopy (EDS) spectra of Ni-P_4Mo_6/GO and Co-P_4Mo_6/GO (Fig. 1 and Fig. S1–S3†) showed that C, P, Mo, N and Ni/Co elements were present and uniformly distributed on the surface of Ni-P_4Mo_6/GO or Co-P_4Mo_6/GO, which indicates that the crystalline materials were successfully loaded onto the surface of GO.

The Ni-P_4Mo_6/GO and Co-P_4Mo_6/GO powders showed the same characteristic peaks in the FT-IR spectrum (Fig. 2a). The characteristic bands in the range of 594–1080 cm^{-1} were assigned to the ν(Mo–O–Mo), ν(Mo–O) and ν(P–O) stretching vibrations of {P_4Mo_6}, respectively. The characteristic peak at 1200–1400 cm^{-1} was attributed to the ν(C=N) stretching vibration in the ligand. The characteristic absorption peaks at 1500–1600 cm^{-1} and 1693 cm^{-1} were attributed to the ν(C=C) stretching vibration and ν(C=O) stretching vibration of GO and the ligand in the compound, respectively.

Single-crystal X-ray diffraction analysis (Table S1†) showed that Ni-P_4Mo_6 and Co-P_4Mo_6 were isomorphic crystals. Ni-P_4Mo_6/GO and Co-P_4Mo_6/GO were characterized by powder X-ray diffraction (PXRD) (Fig. 2b). The experimental diffraction peak of the composites is consistent with the simulated diffraction peaks of Ni-P_4Mo_6 and Co-P_4Mo_6, respectively, and the characteristic peak at 26.18° was attributed to GO, indicating that the crystalline material was successfully compounded with GO. In addition, the elemental composition and valence state of Ni-P_4Mo_6/GO and Co-P_4Mo_6/GO composites were measured by X-ray photoelectron spectroscopy (XPS) (Fig. 3 and Fig. S4†). The XPS full spectra (Fig. 3a) confirmed the presence of Ni/Co, Mo, C, P, O, and N in Ni-P_4Mo_6/GO and Co-P_4Mo_6/GO, respectively. From the XPS fine spectrum of Ni-P_4Mo_6/GO (Fig. 3b), it can be seen that in the Ni 2p spectrum, the 856.5 eV and 873.5 eV peaks were attributed to Ni $2p_{3/2}$ and Ni $2p_{1/2}$, and the 862.5 eV and 880.5 eV characteristic peaks were attributed to Ni $2p_{3/2}$ and Ni $2p_{1/2}$ satellite peaks,[60] indicating that the Ni element in Ni-P_4Mo_6/GO is Ni^{2+}. The fine spectrum of Mo 3d in Fig. 3c shows that the characteristic peaks at 231.7 eV and 234.7 eV belong to Mo $3d_{5/2}$ and Mo $3d_{1/2}$, indicating that the Mo element in Ni-P_4Mo_6/GO is Mo^{5+}.[61] The characteristic peaks at 398.3 eV and 399.5 eV in the N 1s spectrum belonged to the imidazole nitrogen in the organic ligand (Fig. 3d). The C 1s spectrum showed three

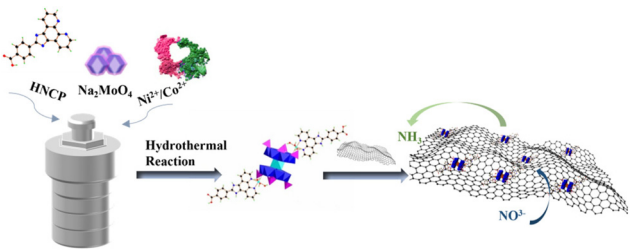

Scheme 1 Synthetic procedure for Ni-P_4Mo_6/GO and Co-P_4Mo_6/GO composites.

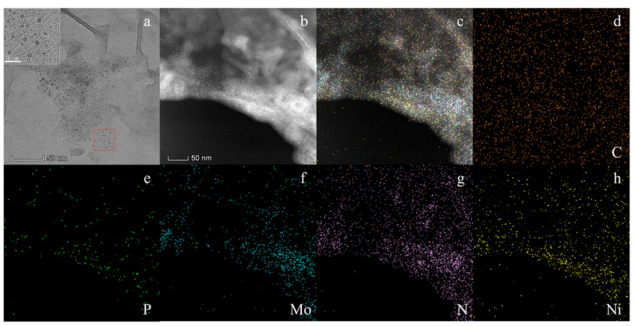

Fig. 1 (a–b) TEM of Ni-P_4Mo_6/GO. (c–h) Element mapping of images of Ni-P_4Mo_6/GO.

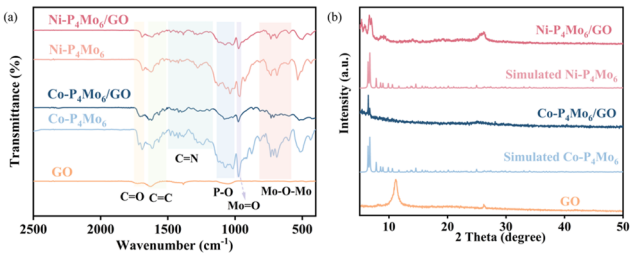

Fig. 2 (a) XRD spectra of Ni-P_4Mo_6/GO and Co-P_4Mo_6/GO. (b) FTIR spectra of Ni-P_4Mo_6/GO and Co-P_4Mo_6/GO.

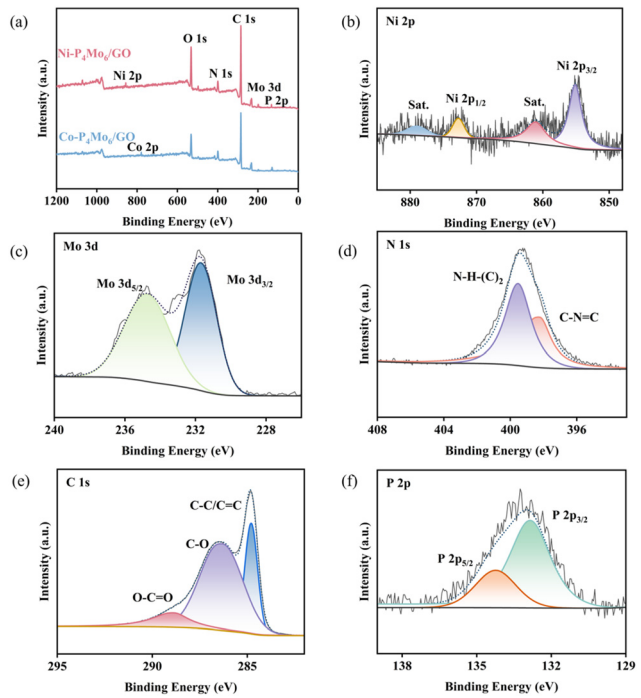

Fig. 3 (a) XPS survey spectra of Ni-P_4Mo_6/GO and Co-P_4Mo_6/GO. High-resolution XPS spectra of (b) Ni 2p, (c) Mo 3d, (d) N 1s, (e) C 1s, and (f) P 2p.

peaks, 284.8, 286.4, and 288.9 eV corresponding to C–C/C=C, C–O, and O–C=O, respectively (Fig. 3e). The characteristic peaks of P 2p at 132.8 and 134.2 eV were attributed to P $2p_{3/2}$ and P $2p_{5/2}$ (Fig. 3f).

The nitrogen adsorption–desorption isotherms of Ni-P_4Mo_6/GO, Co-P_4Mo_6/GO and GO samples were measured (Fig. 4). The results indicate that the specific surface areas of Ni-P_4Mo_6/GO and Co-P_4Mo_6/GO are 23.3 $m^2\ g^{-1}$ and 18.0 $m^2\ g^{-1}$, respectively, which are significantly higher than the specific surface area of GO (1.26 $m^2\ g^{-1}$), which proves the successful loading of the sample. Simultaneously, the higher specific surface area obtained after loading can increase the contact area between the catalyst and the electrolyte, which improves the electrocatalytic performance of the material.[62]

3.3 Electrochemical e-NO_3RR measurement

The e-NO_3RR study was carried out in a typical three-electrode system with an H-type electrolytic cell. Prior to all measurements, high-purity Ar was continuously purged through the cathode compartment at a flow rate of 150 mL min^{-1} for a minimum of 30 minutes to eliminate N_2 from both the electrolyte and the reactor. The measured potentials in this study were calibrated to the RHE scale using the following equation: E (*vs.* RHE) = E (*vs.* Ag/AgCl) + 0.197 + 0.059 × pH, and all the potentials were referenced to reversible hydrogen electrode (*vs.* RHE) potentials. Ammonia production was analyzed by indophenol blue spectrophotometry,[63] and by-product nitrite was analyzed by naphthalene ethylenediamine hydrochloride spectrophotometry (Fig. S5–S8†).[64]

3.3.1 Electrochemical e-NO_3RR under acidic conditions. The linear sweep voltammetry (LSV) curves of Ni-P_4Mo_6/GO and Co-P_4Mo_6/GO were tested under the conditions of 0.1 M $NaNO_3$ + 0.05 M H_2SO_4 (with nitrate) and 0.05 M H_2SO_4 (without nitrate) (Fig. S9a†). The LSV curves reveal that Ni-P_4Mo_6/GO and Co-P_4Mo_6/GO exhibit significantly greater current densities when NO_3^- is present than those in its absence, indicating that Ni-P_4Mo_6/GO and Co-P_4Mo_6/GO have an e-NO_3RR catalytic activity. The corresponding chronoamperometric (j–t) curves of Ni-P_4Mo_6/GO and Co-P_4Mo_6/GO at different potentials were tested (Fig. S9b and S9c†), showing that there is an increase in current density as the potential shifted from −0.3 V to −0.7 V *vs.* RHE. The reduction products were measured quantitatively by UV–vis spectrophotometry (Fig. S9d and S9e†). From Fig. 5a and b, it can be observed that Ni-P_4Mo_6/GO exhibits the best e-NO_3RR performance, with an NH_3 yield of 2.62 mg h^{-1} $mg^{-1}_{cat.}$ (−0.6 V *vs.* RHE) and an FE of 83.9% (−0.5 V *vs.* RHE). Co-P_4Mo_6/GO also achieved certain e-NO_3RR performance, with the highest NH_3 yield of 1.63 mg h^{-1} $mg^{-1}_{cat.}$ (−0.7 V *vs.* RHE) and FE of 85.3% (−0.5 V *vs.* RHE).

3.3.2 Electrochemical e-NO_3RR under neutral conditions. The e-NO_3RR test results of the samples under the above-mentioned acidic conditions could be partially affected by the competitive HER. To further explore the catalytic performance of the catalysts, the e-NO_3RR test under neutral conditions was also performed (0.1 M $NaNO_3$ + 0.1 M Na_2SO_4). The LSV curve test results show that (Fig. 6a), the current density of Ni-P_4Mo_6/GO is higher than that of Co-P_4Mo_6/GO at the same voltage, indicating that its catalytic activity is better. The current density of Ni-P_4Mo_6/GO and Co-P_4Mo_6/GO in the electrolyte increases with the increase in potential (Fig. S10a and S10b†). Compared to Co-P_4Mo_6/GO (NH_3 yield: 4.23 mg h^{-1} $mg^{-1}_{cat.}$ at −1.3 V *vs.* RHE; FE: 65.1% at −0.9 V *vs.* RHE), Ni-

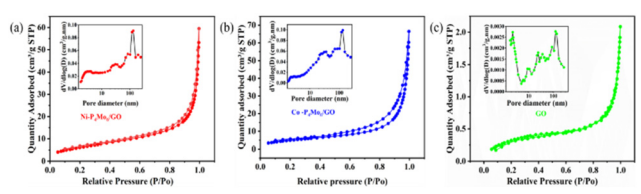

Fig. 4 Nitrogen adsorption–desorption isotherms and corresponding pore-size distribution curves of (a) Ni-P_4Mo_6/GO, (b) Co-P_4Mo_6/GO, and (c) GO.

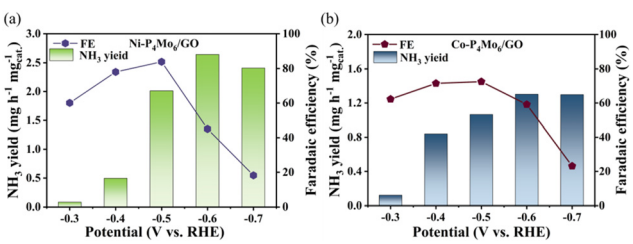

Fig. 5 NH_3 yield rate and FE of (a) Ni-P_4Mo_6/GO and (b) Co-P_4Mo_6/GO.

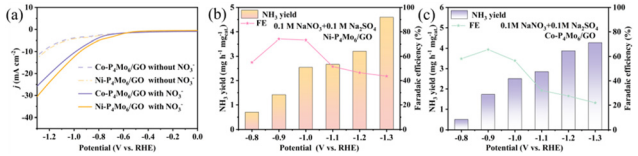

Fig. 6 (a) LSV curves of Ni-P_4Mo_6/GO and Co-P_4Mo_6/GO. NH_3 yield and FE of (b) Ni-P_4Mo_6/GO and (c) Co-P_4Mo_6/GO.

P_4Mo_6/GO (NH_3 yield: 4.52 mg h^{-1} $mg^{-1}_{cat.}$ at −1.3 V *vs.* RHE; FE: 74.1% at −0.9 V *vs.* RHE) exhibits a better catalytic activity (Fig. S10c, S10d† and Fig. 6b, c). In comparison with the electrocatalytic nitrate synthesis ammonia performance under acidic conditions, the performance of catalysts is significantly improved.

3.3.3 Electrochemical e-NO_3RR at different concentrations of NO_3^- electrolytes. To explore how varying nitrate concentrations influence the catalytic activity, Ni-P_4Mo_6/GO, which exhibited better performance in the aforementioned measurement results, was used as the catalyst for further study. The LSV curves of Ni-P_4Mo_6/GO at different concentrations of the NO_3^- electrolyte (10 mM, 0.1 M, 0.2 M, 0.3 M, 0.4 M, 0.5 M and 0.6 M) were further compared (Fig. S11†). The findings show that higher NO_3^- levels lead to a gradual increase in current density, and the initial potential of the reaction shifts to the positive direction, which demonstrates enhanced kinetic accessibility of the nitrate hydrodeoxygenation pathway, facilitating efficient ammonia generation through optimized proton-coupled electron transfer processes.[65]

The best NH_3 yield rate and FE of Ni-P_4Mo_6/GO in electrolyte with different NO_3^- concentrations are shown in Fig. 7 and Table S2.† At a nitrate concentration of 10 mM, an NH_3 yield of Ni-P_4Mo_6/GO is 1.05 mg h^{-1} $mg^{-1}_{cat.}$ (−1.2 V *vs.* RHE) and the FE is only 45.2% (−0.9 V *vs.* RHE) (Fig. 7a). This may be attributed to the fact that when the concentration of nitrate is too low, the e-NO_3RR is inhibited and the performance of the catalyst is reduced.

Then, the electrocatalytic test of Ni-P_4Mo_6/GO was further compared in an electrolyte containing 0.1 to 0.6 M of nitrate (Fig. 7b–g). It is important to highlight that as the nitrate concentration increases, the ammonia production rate and FE of Ni-P_4Mo_6/GO show a trend of gradually increasing first (0.1 M to 0.5 M) and then decreasing (0.6 M). When the nitrate concentration is 0.5 M, the highest NH_3 yield is 11.6 mg h^{-1} $mg^{-1}_{cat.}$ (−1.3 V *vs.* RHE), and the best FE is 88.4% (−1.1 V *vs.* RHE), which is at a high level in the current reported electrocatalytic nitrate reduction yield (Table S3†). When the nitrate concentration is 0.6 M, ammonia production and FE all decrease (Fig. 7g), because the concentration of NO_3^- in the solution continues to increase, the current density increases, but the adsorption ability of Ni-P_4Mo_6/GO for NO_3^- tends to saturate. Meanwhile, the transfer of hydrogen is somewhat limited, resulting in a decrease in NH_3 production and FE.[66]

For comparison, the e-NO_3RR tests of Co-P_4Mo_6/GO and GO were also conducted in 0.5 M $NaNO_3$/Na_2SO_4 electrolyte

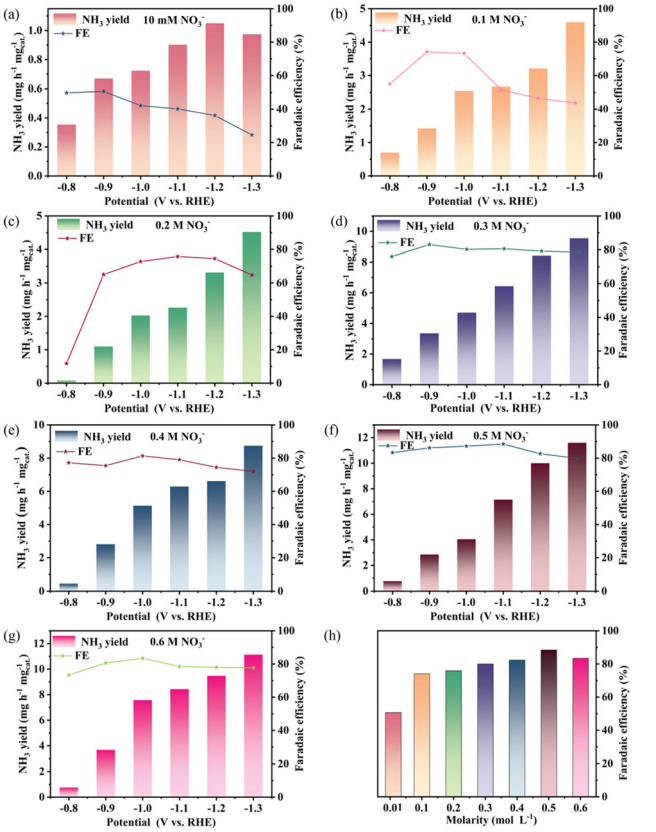

Fig. 7 (a–g) NH_3 yield rate and FE of Ni-P_4Mo_6/GO with different NO_3^- concentrations. (h) FE corresponding to the optimal voltage of Ni-P_4Mo_6/GO at each concentration.

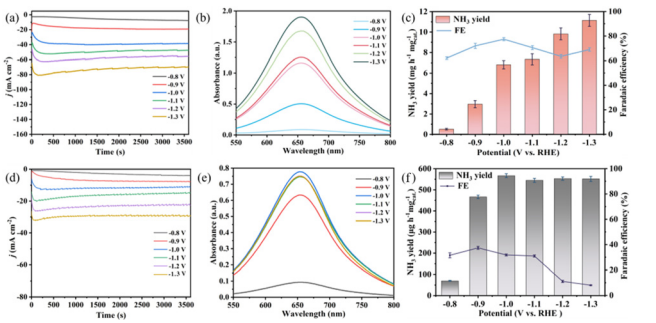

Fig. 8 (a) Chronoamperometric (*j*–*t*) curves of Co-P_4Mo_6/GO. (b) UV-vis absorption spectra of Co-P_4Mo_6/GO. (c) NH_3 yield rate and FE of Co-P_4Mo_6/GO. (d) Corresponding chronoamperometric (*j*–*t*) curves of GO. (e) UV-vis absorption spectra of GO. (f) NH_3 yield rate and FE of GO.

(Fig. 8). The results indicate that Co-P_4Mo_6/GO also has positive e-NO_3RR performance (the NH_3 yield of 11.1 mg h^{-1} $mg^{-1}_{cat.}$ (−1.1 V *vs.* RHE) and FE of 78.5% (−1.0 V *vs.* RHE)) (Fig. 8c). The NH_3 yield of 0.55 mg h^{-1} $mg^{-1}_{cat.}$ (−1.1 V *vs.* RHE) and the FE of 39.2% (−0.9 V *vs.* RHE) are obtained for GO, which exhibits almost minor e-NO_3RR activity compared with the composite (Fig. 8f).

Since the e-NO_3RR to NH_3 is an intricate process requiring an eight-electron transfer, the by-products include NO_2^-, which is also studied by hydrochloric acid naphthalene ethylenediamine spectroscopy analysis (Fig. S12†). We observe that the FE values for NO_2^- are below 10% (Fig. 9a), with the maximum yield reaching only 0.3 mg h^{-1} $mg^{-1}_{cat.}$, suggesting that Ni-P_4Mo_6/GO demonstrates strong selectivity during the nitrate-to-ammonia conversion process.

Electrochemical impedance spectroscopy (EIS) is widely acknowledged as an effective approach for investigating catalytic kinetics. The Nyquist plots[67] and Bode plots of Ni-P_4Mo_6/GO, Co-P_4Mo_6/GO and GO were performed (Fig. 9b and Fig. S13†). From the Nyquist plots, the linear slope of GO itself is the smallest, indicating that the diffusion resistance of GO is large, which is not conducive to the e-NO_3RR dynamic process. After the crystal material was loaded, the slope increases and the diffusion resistance decreases, which is consistent with the high e-NO_3RR performance of Ni-P_4Mo_6/GO and Co-P_4Mo_6/GO. Ni-P_4Mo_6/GO demonstrates minimal charge transfer resistance and optimal electron transport efficiency, confirming that the Faraday process between it and the electrolyte interface was faster. The C_{dl} value of Ni-P_4Mo_6/GO is 3.7 mF cm^{-2}, and the C_{dl} value of Co-P_4Mo_6/GO is 3.1 mF cm^{-2}, indicating that Ni-P_4Mo_6/GO has better electrochemical performance (Fig. S14†).

Good stability is essential for catalysts. After 24 hours of continuous electrolysis, the XRD pattern, FTIR spectrum and XPS spectra of the Ni-P_4Mo_6/GO composite showed that the structure of the material did not change (Fig. 10a, b and Fig. S15†). This reveals that the material structure did not change. Under the optimal conditions for ammonia synthesis (−1.1 V *vs.* RHE, 0.5 M $NaNO_3$ + 0.1 M Na_2SO_4 electrolyte), the current density of the catalyst remained basically unchanged during continuous electrolysis for 24 h (Fig. 10). The NH_3 yield and FE of Ni-P_4Mo_6/GO changed in a small range after 24 cycles of electrocatalytic tests under the same conditions, which indicates that the catalyst Ni-P_4Mo_6/GO exhibits good stability.

A set of control experiments were conducted to verify the origin of the produced NH_3: (1) Ni-P_4Mo_6/GO served as the working electrode in an Ar-saturated blank solution lacking $NaNO_3$, and can hardly detect ammonia after electrolysis (Fig. 11a); (2) using bare carbon cloth as the working electrode, very little ammonia was produced after electrolysis for 1 h in a 0.1 M Na_2SO_4 solution with $NaNO_3$. To verify the origin of NH_3, N-isotope labeling experiments were conducted. When $Na^{14}NO_3$ served as the nitrogen source, the ^{1}H NMR spectrum of the electrolyte exhibited three distinct characteristic peaks of $^{14}NH_4^+$ following the e-NO_3RR test. When $Na^{15}NO_3$ was used as the nitrogen source, the ^{1}H NMR spectrum of the electrolyte after the electrocatalytic test showed two characteristic peaks of $^{15}NH_4^+$ (Fig. 11b).[68] The above-mentioned findings provide strong evidence that all the ammonia is derived from the conversion of NO_3^- on Ni-P_4Mo_6/GO.

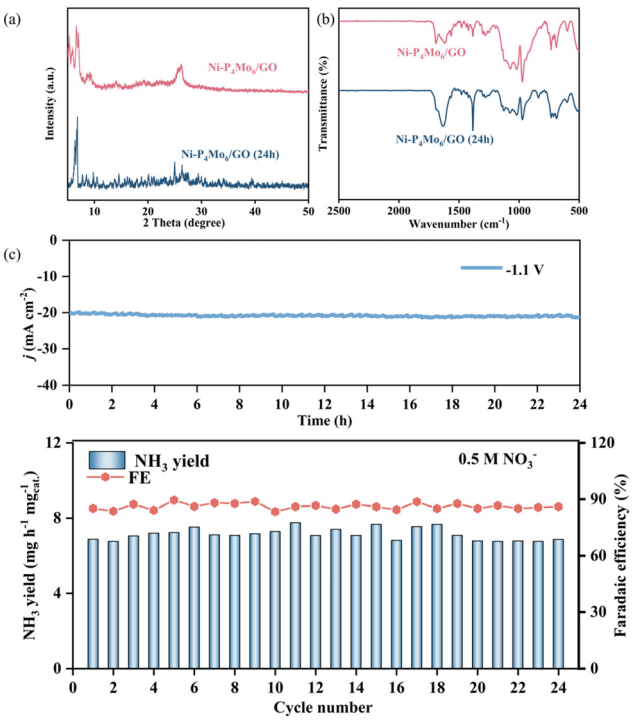

Fig. 10 (a) Comparison of the XRD patterns of Ni-P_4Mo_6/GO after continuous electrolysis for 24 hours. (b) FT-IR spectra of Ni-P_4Mo_6/GO before and after continuous electrolysis for 24 hours. (c) Corresponding chronoamperometric (j–t) curves for 24 h continuous electrolysis at −1.1 V *vs.* RHE and NH_3 yield rate and FE with different cycles.

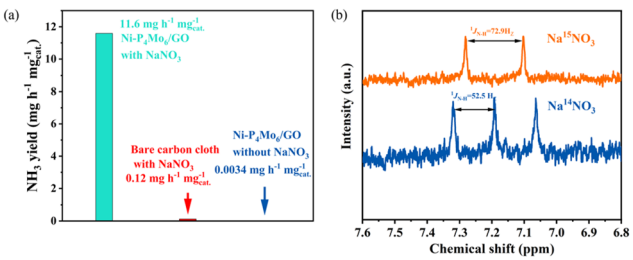

Fig. 11 (a) NH_3 yield rate of Ni-P_4Mo_6/GO in 0.1 M Na_2SO_4 with or without $NaNO_3$, respectively, and blank carbon paper in 0.1 M Na_2SO_4 solution with $NaNO_3$. (b) ^{1}H NMR spectra of the electrolyte after 1 h of NO_3RR testing at −1.1 V *vs.* RHE with $^{14}NO_3^-$ and $^{15}NO_3^-$ as the N source, respectively.

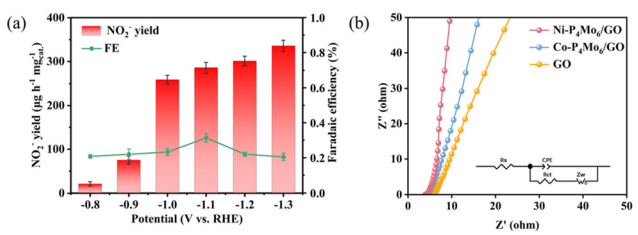

Fig. 9 (a) NO_2^- yield rate and FE of Ni-P_4Mo_6/GO. (b) Electrochemical impedance spectra of Ni-P_4Mo_6/GO, Co-P_4Mo_6/GO and GO.

4. Conclusions

In this work, two crystalline materials were synthesized using a one-pot mode and loaded with GO to obtain two composites (Ni-P_4Mo_6/GO and Co-P_4Mo_6/GO). The systematic optimization of electrolyte composition and nitrate feed concentrations was conducted to elucidate their synergistic influence on electrocatalytic activity, selectivity, and stability metrics in the nitrate reduction reaction. In the neutral electrolyte, the catalytic activity of Ni-P_4Mo_6/GO and Co-P_4Mo_6/GO was significantly improved and superior to some similar catalysts owing to the combined influence of the electron-donating capacity of the $\{P_4Mo_6\}$ unit, good catalytic activity of Ni/Co, and the excellent charge transport ability of the graphene substrate. It is worth noting that the NH_3 yield (11.6 mg h^{-1} $mg^{-1}_{cat.}$) and FE (88.4%) of Ni-P_4Mo_6/GO are higher than those of Co-P_4Mo_6/GO (NH_3 yield of 11.1 mg h^{-1} $mg^{-1}_{cat.}$, FE of 78.5%). This work establishes a transformative design paradigm for polyoxometalate-derived electrocatalysts, offering mechanistic insights and synthetic protocols that advance the frontier of e-NO_3RR technologies.

Author contributions

Nan Zhao: data curation, formal analysis, investigation methodology, software, writing – original draft. Xinming Wang: conceptualization, data curation, formal analysis, funding acquisition, methodology, resources, supervision, writing – review & editing. Shuang Rong: software, validation. Qiushuang Jiang: conceptualization, methodology. Haoyun Li: data curation, formal analysis. Haijun Pang: funding acquisition, software, validation. Huiyuan Ma: conceptualization, data curation, formal analysis, methodology, resources, supervision.

Data availability

All relevant data are available within the manuscript and its additional files.

Conflicts of interest

There are no conflicts to declare.

Acknowledgements

This work was supported by the National Natural Science Foundation of China (22171059), the ZR2022MB096 project funded by the Shandong Provincial Natural Science Foundation, and Heilongjiang Provincial Natural Science Foundation of China (LH2024B015).

References

1 F. Lü, S. Zhao, R. Guo, J. He, X. Peng, H. Bao, J. Fu, L. Han, G. Qi, J. Luo, X. Tang and X. Liu, *Nano Energy*, 2019, **61**, 420–427.
2 Z. Mo, J. Mu and B. Liu, *J. Electroanal. Chem.*, 2024, **969**, 118533.
3 H. Wang, J. Huang, J. Cai, Y. Wei, A. Cao, B. Liu and S. Lu, *Small Methods*, 2023, **7**, 00169.
4 S. L. Foster, S. I. P. Bakovic, R. D. Duda, S. Maheshwari, R. D. Milton, S. D. Minteer, M. J. Janik, J. N. Renner and L. F. Greenlee, *Nat. Catal.*, 2018, **1**, 490–500.
5 S. Feng, W. Gao, H. Cao, J. Guo and P. Chen, *Acta Chim. Sin.*, 2020, **78**, 916.
6 Z. Ni, N. Liu, C. Zhao and L. Mi, *Polyoxometalates*, 2024, **3**, 9140044.
7 Z. Fang, P. Wu, Y. Qian and G. Yu, *Angew. Chem., Int. Ed.*, 2020, **60**, 4275–4281.
8 Q. Song, M. Li, J. Li, S. Zhang, L. Yang, X. Chen, F. Meng and X. Liu, *Chem. Eng. J.*, 2022, **430**, 133152.
9 J. Zheng, Y. Lyu, M. Qiao, R. Wang, Y. Zhou, H. Li, C. Chen, Y. Li, H. Zhou, S. P. Jiang and S. Wang, *Chem*, 2019, **5**, 617–633.
10 X. Wang, M. Yang, C. J. Gómez-García, X. Cao, Z. Jin, H. Ma, H. Pang and G. Yang, *ACS Sustainable Chem. Eng.*, 2025, **13**, 1708–1718.
11 S. P. Wallbridge, K. Lawson, A. E. Catling, C. A. Kirk and S. E. Dann, *Dalton Trans.*, 2022, **51**, 18010–18023.
12 G. Duan, Y. Chen, Y. Tang, K. A. M. Gasem, P. Wan, D. Ding and M. Fan, *Prog. Energy Combust. Sci.*, 2020, **81**, 100860.
13 H. Jiang, T. Li, Y. Gao, J. Fan, D. Gan, S. Yuan, L. Hong, Y. Feng, J. Sun, Q. Song, T. Zhang, A. R. Jalili, P. J. Cullen and R. Zhou, *J. Energy Chem.*, 2025, **105**, 630–668.
14 X. Xue, R. Chen, C. Yan, P. Zhao, Y. Hu, W. Zhang, S. Yang and Z. Jin, *Nano Res.*, 2019, **12**, 1229–1249.
15 A. Ma, J. Gui, Y. Huang and Y. Yu, *Nano Res.*, 2024, **17**, 7824–7829.
16 Y. Zhang, J. Xiong, B. Liu and S. Yan, *Cell Rep. Phys. Sci.*, 2024, **5**, 101994.
17 J.-Y. Fang, J.-L. Fan, S.-B. Liu, S.-P. Sun and Y.-Y. Lou, *Materials*, 2023, **16**, 4000.
18 Q. Zhou, X. Wang, S. Rong, G. Li, Q. Jiang, H. Pang and H. Ma, *Inorg. Chem.*, 2025, **64**, 5291–5301.
19 X. Lu, J. Yu, J. Cai, Q. Zhang, S. Yang, L. Gu, G. I. N. Waterhouse, S.-Q. Zang, B. Yang and S. Lu, *Cell Rep. Phys. Sci.*, 2022, **3**, 100961.
20 Y. Xu, Y. Sheng, M. Wang, T. Liu, H. Yu, K. Deng, Z. Wang, L. Wang and H. Wang, *J. Mater. Chem. A*, 2022, **10**, 16290–16296.
21 K. Wu, C. Sun, Z. Wang, Q. Song, X. Bai, X. Yu, Q. Li, Z. Wang, H. Zhang, J. Zhang, X. Tong, Y. Liang, A. Khosla and Z. Zhao, *ACS Mater. Lett.*, 2022, **4**, 650–656.
22 J. Yan, P. Liu, J. Li, H. Huang, S. Tong and W. Song, *Chem. Eng. J.*, 2024, **498**, 155108.
23 M. Wang, T. Hu, C. Wang, F. Du, H. Yang, W. Sun, C. Guo and C. M. Li, *Sci. China Mater.*, 2023, **66**, 2750–2758.

24 D. Hao, Z.-g. Chen, M. Figiela, I. Stepniak, W. Wei and B.-J. Ni, *J. Mater. Sci. Technol.*, 2021, **77**, 163–168.
25 Y. Xu, M. Wang, K. Ren, T. Ren, M. Liu, Z. Wang, X. Li, L. Wang and H. Wang, *J. Mater. Chem. A*, 2021, **9**, 16411–16417.
26 Z. A. Jonoush, A. Rezaee and A. Ghaffarinejad, *J. Cleaner Prod.*, 2020, **242**, 118569.
27 M. Teng, J. Yuan, Y. Li, C. Shi, Z. Xu, C. Ma, L. Yang, C. Zhang, J. Gao and Y. Li, *J. Colloid Interface Sci.*, 2024, **654**, 348–355.
28 E. Lacasa, P. Cañizares, J. Llanos and M. A. Rodrigo, *J. Hazard. Mater.*, 2012, **213–214**, 478–484.
29 T. Zhang, S. Liu, F. Wang, W. Liu, X. He, Q. Liu, X. Zhang and X. Liu, *Microstructures*, 2024, **4**, 2024043.
30 J. Wang, T. Feng, J. Chen, V. Ramalingam, Z. Li, D. M. Kabtamu, J.-H. He and X. Fang, *Nano Energy*, 2021, **86**, 106088.
31 M. Jiang, J. Su, X. Song, P. Zhang, M. Zhu, L. Qin, Z. Tie, J.-L. Zuo and Z. Jin, *Nano Lett.*, 2022, **22**, 2529–2537.
32 H.-Y. Kwon, S. E. Braley, J. P. Madriaga, J. M. Smith and E. Jakubikova, *Dalton Trans.*, 2021, **50**, 12324–12331.
33 S. Li, Z. Zhao, T. Ma, P. Pachfule and A. Thomas, *Angew. Chem., Int. Ed.*, 2021, **61**, e202112298.
34 S. Li, C. Cheng, A. Sagaltchik, P. Pachfule, C. Zhao and A. Thomas, *Adv. Funct. Mater.*, 2018, **29**, 1807419.
35 C.-Y. Sun, W. Li, K. Wang, W.-J. Zhou and H.-Q. Wang, *Rare Met.*, 2024, **43**, 1845–1866.
36 L. Wang, M. Li, X. Liu, C. Feng, N. Chen, X. Ma and G. Ding, *J. Electrochem. Soc.*, 2017, **164**, E326–E331.
37 D. He, Y. Li, H. Ooka, Y. K. Go, F. Jin, S. H. Kim and R. Nakamura, *J. Am. Chem. Soc.*, 2018, **140**, 2012–2015.
38 D. Zhao, J. Yao, C. Ma, A. Wang, H. Xie, J. Zhao, J. Yan, K. Zhu, Y. Zhu, D. Cao and G. Wang, *J. Power Sources*, 2024, **592**, 233945.
39 H. Li, M. Tu, Y. Fang, T. Hao and B. Wang, *ACS Appl. Nano Mater.*, 2023, **6**, 18238–18246.
40 Y.-T. Xu, Y. Han, D. K. Sam and Y. Cao, *J. Mater. Chem. A*, 2022, **10**, 22390–22398.
41 W. Zheng, L. Zhu, Z. Yan, Z. Lin, Z. Lei, Y. Zhang, H. Xu, Z. Dang, C. Wei and C. Feng, *Environ. Sci. Technol.*, 2021, **55**, 13231–13243.
42 N. I. Gumerova and A. Rompel, *Nat. Rev. Chem.*, 2018, **2**, 018–0112.
43 M. Yang, X. Wang, C. J. Gómez-García, Z. Jin, J. Xin, X. Cao, H. Ma, H. Pang, L. Tan, G. Yang and Y. Kan, *Adv. Funct. Mater.*, 2023, **33**, 2214495.
44 M. R. Horn, A. Singh, S. Alomari, S. Goberna-Ferrón, R. Benages-Vilau, N. Chodankar, N. Motta, K. Ostrikov, J. MacLeod, P. Sonar, P. Gomez-Romero and D. Dubal, *Energy Environ. Sci.*, 2021, **14**, 1652–1700.
45 A. V. Anyushin, A. Kondinski and T. N. Parac-Vogt, *Chem. Soc. Rev.*, 2020, **49**, 382–432.
46 G. Yang, H. Liu, S. Zhang, Y. Yang, K. Li, H. Li, Y. Liu and H. Zang, *Inorg. Chem.*, 2024, **63**, 22955–22961.
47 G. Yang, J. Cao, Y. Xiao, Q. Hu, H. Liu, X. Cao, K. Li, Y. Zhang and X. Li, *Inorg. Chem.*, 2025, **64**, 1041–1047.
48 J.-X. Liu, X.-B. Zhang, Y.-L. Li, S.-L. Huang and G.-Y. Yang, *Coord. Chem. Rev.*, 2020, **414**, 213260.
49 Q. Hu, K. Li, X. Chen, Y. Liu and G. Yang, *Polyoxometalates*, 2024, **3**, 9140048.
50 L. Guo, L. He, Q. Zhuang, B. Li, C. Wang, Y. Lv, J. Chu and Y. F. Song, *Small*, 2023, **19**, 07315.
51 M. Khalaji-Verjani and M. Masteri-Farahani, *ACS Appl. Energy Mater.*, 2024, **7**, 6612–6620.
52 L. Yang, Z. Yuan, L. He, L. Han, B. Li and Y. Xu, *Inorg. Chem.*, 2024, **63**, 12564–12571.
53 H.-L. Guo, X.-X. Xing, S.-X. Mao, T. Feng, Y.-H. Fan, Z.-J. Qin, J.-Y. Pang, Y. Bai and D.-B. Dang, *Dalton Trans.*, 2022, **51**, 18090–18098.
54 J.-Q. Niu, W.-T. An, X.-J. Zhang, Y.-Y. Ma and Z.-G. Han, *Chem. Eng. J.*, 2021, **418**, 129408.
55 H.-X. Bi, M.-S. Guo, J. Du, Y.-Y. Ma and Z.-G. Han, *Coord. Chem. Rev.*, 2024, **518**, 216092.
56 J. Wang, S. Wang, Z. Zhang and C. Wang, *J. Environ. Manage.*, 2020, **276**, 111357.
57 X. Ma, M. Li, X. Liu, L. Wang, N. Chen, J. Li and C. Feng, *Chem. Eng. J.*, 2018, **348**, 171–179.
58 W. Yu, L. Sisi, Y. Haiyan and L. Jie, *RSC Adv.*, 2020, **10**, 15328–15345.
59 N. M. Mahmoodi, M. Oveisi and E. Asadi, *J. Cleaner Prod.*, 2019, **211**, 198–212.
60 Q. Sheng, Y. Wang, P. Zhang, Y. Jiang, J. Zhang, Q. Liu, Q. Chang, Y. Yao, X. Liao, Z. Li, S. Lyu and Y. Qin, *Appl. Surf. Sci.*, 2024, **666**, 160369.
61 Y.-Q. Zhang, L.-Y. Zhou, Y.-Y. Ma, K. Dastafkan, C. Zhao, L.-Z. Wang and Z.-G. Han, *Chem. Sci.*, 2021, **12**, 1886–1890.
62 Y. Hou, D. Chai, B. Li, H. Pang, H. Ma, X. Wang and L. Tan, *ACS Appl. Mater. Interfaces*, 2019, **11**, 20845–20853.
63 Y. Zhao, R. Shi, X. Bian, C. Zhou, Y. Zhao, S. Zhang, F. Wu, G. I. N. Waterhouse, L. Z. Wu, C. H. Tung and T. Zhang, *Adv. Sci.*, 2019, **6**, 02109.
64 Q.-H. Wang, L.-J. Yu, Y. Liu, L. Lin, R.-g. Lu, J.-p. Zhu, L. He and Z.-L. Lu, *Talanta*, 2017, **165**, 709–720.
65 L. Bai, F. Franco, J. Timoshenko, C. Rettenmaier, F. Scholten, H. S. Jeon, A. Yoon, M. Rüscher, A. Herzog, F. T. Haase, S. Kühl, S. W. Chee, A. Bergmann and R. C. Beatriz, *J. Am. Chem. Soc.*, 2024, **146**, 9665–9678.
66 Q. Hu, K. Yang, O. Peng, M. Li, L. Ma, S. Huang, Y. Du, Z.-X. Xu, Q. Wang, Z. Chen, M. Yang and K. P. Loh, *J. Am. Chem. Soc.*, 2023, **146**, 668–676.
67 Z. Feng, G. Li, X. Wang, C. J. Gómez-García, J. Xin, H. Ma, H. Pang and K. Gao, *Chem. Eng. J.*, 2022, **445**, 136797.
68 K. Kamiya, K. Hashimoto and S. Nakanishi, *ChemElectroChem*, 2014, **1**, 858–862.